Featured in Physics

Massively Multiplexed Nanoscale Magnetometry with Diamond Quantum Sensors

Kai-Hung Cheng,[1] Zeeshawn Kazi,[1] Jared Rovny,[1] Bichen Zhang,[1] Lila S. Nassar,[2] Jeff D. Thompson,[1] and Nathalie P. de Leon[1,*]

[1]*Princeton University, Department of Electrical and Computer Engineering, Princeton, New Jersey 08544, USA*

[2]*Princeton University, Department of Physics, Princeton, New Jersey 08544, USA*

(Received 10 September 2024; accepted 22 May 2025; published 14 July 2025)

Single nitrogen vacancy (NV) centers in diamond have been used extensively for high-sensitivity nanoscale sensing, but conventional approaches use confocal microscopy to measure individual centers sequentially, limiting throughput and access to nonlocal physical properties, where simultaneous, high-fidelity measurement of multiple centers is required. Here, we design and implement a multiplexed NV sensing platform that allows us to read out many single NV centers simultaneously using a low-noise camera. Using this platform, we coherently manipulate and read out the spin states of hundreds of individual NV centers in parallel, achieving comparable magnetic field sensitivity to confocal measurements. We also implement a parallelized version of spin-to-charge-conversion readout for low NV center spin state readout noise and use it to demonstrate multiplexed covariance magnetometry, in which we measure ten two-point magnetic field correlators from five NV centers simultaneously. From these measurements, we demonstrate the quantitative reconstruction of spatially varying magnetic correlations arising from a current-carrying wire. The number of correlators we can measure is limited only by the available laser power, opening the door to massively multiplexed covariance magnetometry. In contrast to scanning probes for imaging spatially varying magnetic fields, our approach measures the temporal dynamics of the magnetic field at many precisely defined positions simultaneously, from which the local noise spectrum and nonlocal properties such as correlation functions can be computed. This high-fidelity readout platform will find immediate applications in studying condensed matter phenomena that are characterized by the noise spectrum or correlation functions, including quantum phase transitions, dynamics far from equilibrium, magnetic order, and correlated electron phenomena.

DOI: 10.1103/t8fz-3tzs

Subject Areas: Condensed Matter Physics, Quantum Information

I. INTRODUCTION

Nitrogen vacancy (NV) centers in diamond have long spin coherence times across a wide range of temperatures combined with optical spin initialization and readout, enabling broad applications in nanoscale sensing of quantities such as magnetic field, electric field, and temperature [1–7]. NV centers are typically deployed either as individual sensors in bulk diamond [1–3,5,8,9], scanning tip geometries [10–12], or in dense ensembles of NV centers that are not individually resolvable [7,13–16]. Resolvable NV centers offer nanometer sensing volumes [17] and high sensitivity even for NV centers within a few nanometers of the surface with proper surface preparation [18,19] but suffer from slow measurements due to the high readout noise of the NV center spin state [20,21]. NV center ensembles offer fast, high-fidelity measurements by averaging over the signal measured by many NV centers [13,14,21,22] at the cost of micron-scale spatial averaging imposed by the diffraction limit.

In this work, we demonstrate a multiplexed NV sensing platform that combines the best of these modalities, realizing parallel, wide-field measurements of many individually resolvable NV centers using a low-noise camera. We first demonstrate parallel continuous-wave optically detected magnetic resonance of hundreds of resolvable NV centers, achieving a magnetic field sensitivity within a factor of 5 of confocal measurements of single centers in the same sample. We extend this technique to spatially resolved spin measurements, performing parallel relaxometry (T_1 measurements) of 70 NV centers. Next, we demonstrate enhanced parallel spin readout by implementing spin-to-charge conversion (SCC) using a spatial light

*Contact author: npdeleon@princeton.edu

Published by the American Physical Society under the terms of the Creative Commons Attribution 4.0 International license. Further distribution of this work must maintain attribution to the author(s) and the published article's title, journal citation, and DOI.

modulator (SLM) to focus a high-power ionization laser onto multiple NV centers simultaneously. We realize efficient ionization and multiplexed single-shot charge-state readout with a fidelity of 88%, which enables multiplexed SCC spin readout with low readout noise, around 10 times the quantum projection noise limit. This architecture allows us to measure magnetic field correlations between four individually resolved NV centers in parallel. The scalability of the multiplexed SCC is limited by the ionization laser power, and we expect that these techniques can be extended to hundreds of NV centers in future work, enabling parallel nanoscale sensing of nonlocal properties at many length scales [23]. Our platform will find immediate applications to studying condensed matter phenomena that are characterized by the noise spectrum or correlation functions [23], including quantum phase transitions [24], dynamics far from equilibrium [25–27], magnetic order [28,29], and correlated electron phenomena [30].

II. MASSIVELY MULTIPLEXED NV CENTER MEASUREMENTS

Our multiplexing platform [Fig. 1(a)] uses an electron-multiplying charge-coupled device (EMCCD) camera to detect NV center fluorescence and a microwave printed-circuit board in front of the objective to deliver microwave (MW) excitation [31]. Using cw wide-field green (532 nm) excitation, we image several hundred NV centers with approximately 2 s of integration time on the camera [Fig. 1(b)]. We demonstrate parallel spin control and readout by measuring the optically detected magnetic resonance (ODMR) spectrum of all the NV centers in the field of view. We simultaneously measure several hundred ODMR spectra in parallel [Fig. 2(a)] by recording the fluorescence emitted by each NV center under cw excitation as a function of applied microwave frequency and normalizing by a reference measurement with no applied microwaves [Fig. 2(b)]. NV centers exist in four possible crystallographic orientations [1], and three distinct

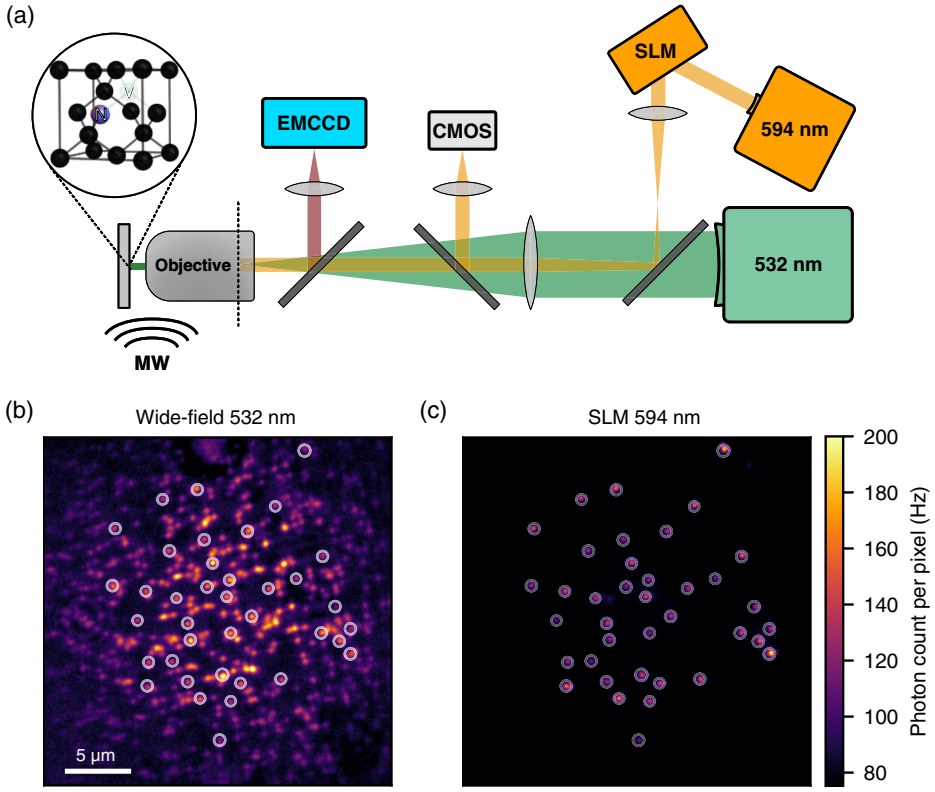


FIG. 1. Multiplexing platform for quantum sensing applications using NV centers in diamond. (a) Diagram of the experiment setup. A green (532 nm) laser is focused to the back focal plane of the objective lens for wide-field excitation of the NV centers. An orange (594 nm) laser is reflected off a SLM with a programmable phase map to generate the laser beam pattern of the selected NV centers at the sample. The SLM plane is relayed onto the back focal plane of the objective lens. The orange laser beam is sampled before the objective lens and imaged onto a CMOS camera for pattern calibration. The fluorescence emitted by the NV centers is imaged onto a low-noise EMCCD camera for readout. Inset: diagram showing the NV center defect in the diamond lattice. (b) A wide-field green laser spot is used for imaging and individual spin measurement using green excitation. (c) An orange laser beam reflected off an SLM generates a pattern of diffraction-limited laser beams at the sample to selectively excite targeted NV centers for high-fidelity readout. The circled NV centers in both images are the same.

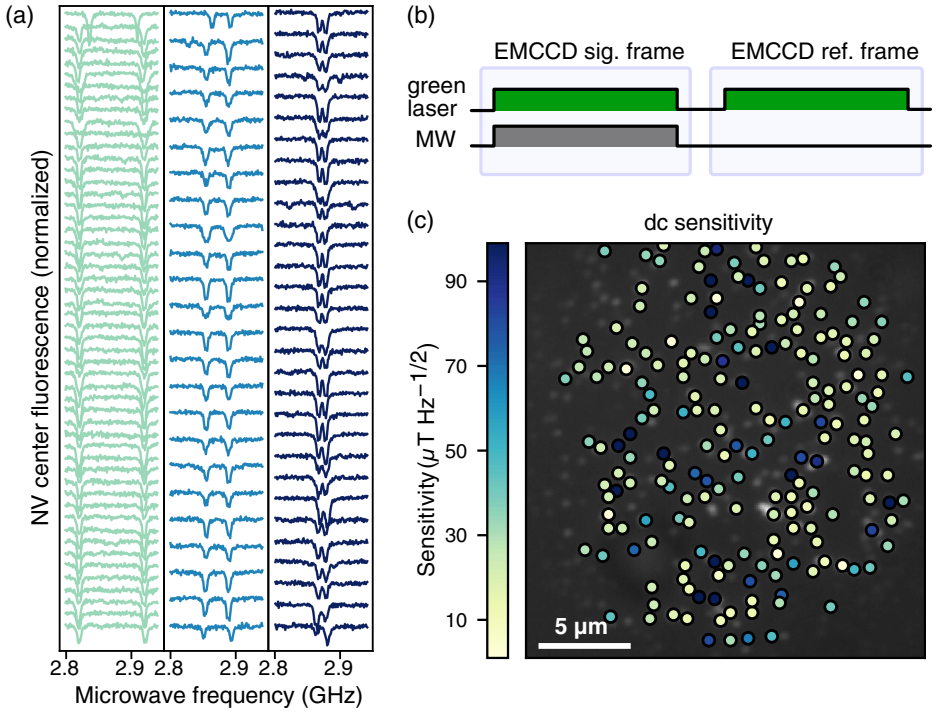


FIG. 2. Multiplexed continuous-wave NV spin measurements. (a) cw ODMR (150 spectra) measured in parallel with wide-field green laser and MW excitation. Different colors of the curves represent different families of crystallographic orientations of the NV centers. Only three distinct orientations are observed here, because two are degenerate under the static magnetic field alignment. (b) Pulse sequence for continuous-wave ODMR measurement. (c) Map of dc magnetic field sensitivity obtained by fitting ODMR spectra and measuring photon count rates for 199 NV centers in parallel. The spatial extent of the map is given by the size of the wide-field excitation spot. Variations in sensitivity are attributed to the presence of ^{13}C nuclei or varying proximal surface inhomogeneities leading to NV charge-state instability.

orientations are observed here [Fig. 2(a), different colors], because two are degenerate under the static magnetic field alignment. From the ODMR spectra, we calculate the dc magnetic field sensitivity of each individual NV center and find the median dc sensitivity is 24 $\mu\mathrm{T\,Hz}^{-1/2}$ [Fig. 2(c)] compared to a median sensitivity of 5.5 $\mu\mathrm{T\,Hz}^{-1/2}$ obtained with confocal measurements of the same diamond sample, where the difference is due to the lower optical intensity per NV center with wide-field excitation (Figs. 7 and 8).

Parallel readout also enables the multiplexed measurement of NV center dynamics. Pulsed measurements are challenging, because the EMCCD camera data transfer time of 10 ms is much longer than the typical readout time of 300 ns, determined by the lifetime of the shelving state [20]. For wide-field pulsed measurements using the camera, we repeat the experiment multiple times while integrating the fluorescence on the camera [Fig. 3(b)] [22,32]. This reduces the overhead of frame transfer time and suppresses the noise from camera readout but lowers the fluorescence contrast between the NV spin states, because the camera also records fluorescence during the spin reinitialization between experiments. With this approach, we are able to measure Rabi oscillations of many NV centers simultaneously [Fig. 3(a)]. We demonstrate the application of parallel pulsed experiments to measure the spin relaxation time T_1 of over 70 NV centers in parallel [Fig. 3(c)]. The measured T_1 times in this sample, which has NV centers implanted within approximately 10 nm of the surface, range from a few hundred microseconds to over 4 ms, consistent with past measurements of similarly prepared samples [18,33].

III. PARALLELIZED SPIN-TO-CHARGE CONVERSION

We next demonstrate multiplexed low-noise readout of the NV center spin state using SCC, which is critical for covariance magnetometry [34] as the time required to measure a magnetic field correlation signal with a given signal-to-noise ratio scales as σ_{R}^4, where σ_{R} is defined as the single-shot spin state readout noise [21]. SCC achieves lower σ_{R} compared to green readout by using a high-power laser pulse to selectively ionize the NV center based on its spin state, followed by a high-fidelity charge-state readout [35]. The selective ionization step typically requires approximately 10 mW of optical power per NV center, so implementing SCC with a wide-field laser beam would require >100 W of power for a 20 × 20 μm region. Thus, to realize multiplexed SCC in a power-efficient manner, we use an SLM to create a programmable pattern of laser

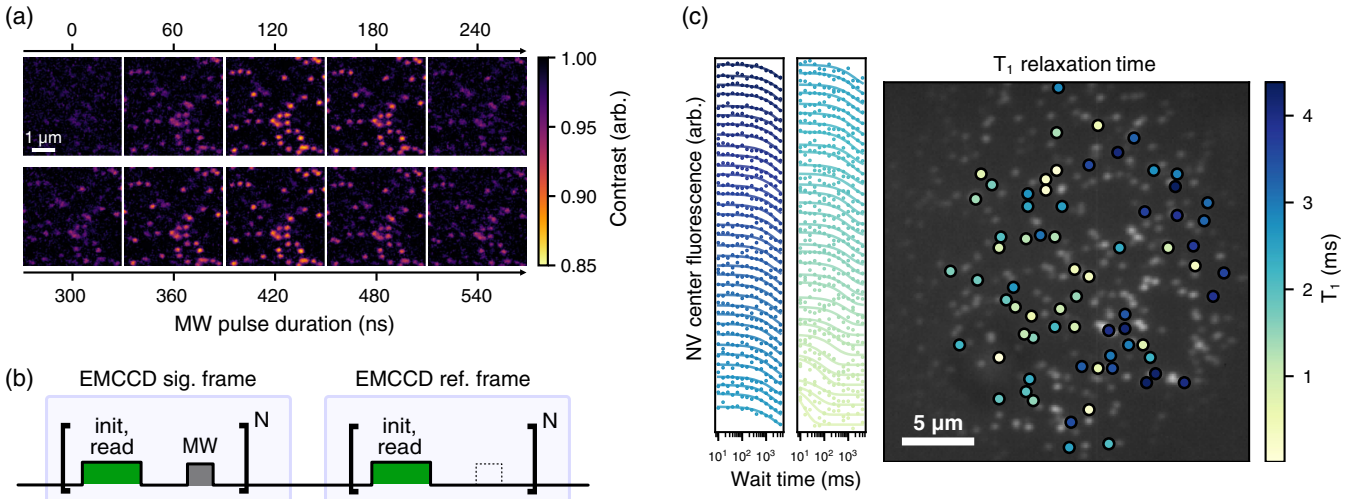


FIG. 3. Multiplexed coherent control and dynamics. (a) Snapshots of a wide-field Rabi oscillation experiment at increasing microwave pulse time. Each image is an average of five million experiment repetitions across 200 camera frames. (b) Pulse sequence for pulsed experiments with EMCCD camera readout. (c) Simultaneous longitudinal spin relaxation (T_1) measurement of the 70 NV centers of a given crystallographic orientation (left), with a map of the fitted longitudinal spin relaxation time T_1 (right).

beams that excite only targeted NV centers [Fig. 1(c)]. For simplicity, we use the same illumination pattern and wavelength (orange, 594 nm) for both ionization and charge-state readout.

We implement multiplexed charge-state readout with the SLM and the camera through the following steps, outlined in Figs. 4(a)–4(c). First, we take an image of all the NV centers using wide-field green excitation to fit the NV center coordinates [Fig. 4(a)]. Second, we run a weighted Gerchberg-Saxton algorithm to generate a phase pattern on the SLM to create the laser spots at targeted NV center locations [Fig. 4(b)] [36]. To read out the charge state, we excite the NV centers with a low-power orange laser and measure the photon counts per exposure by thresholding individual pixels in a region around each NV center and then summing the thresholded counts [Fig. 4(c)]. In this low-photon regime, we binarize the image such that each pixel measures either zero or one photons and do not account for higher per-pixel counts, which allows us to take full advantage of the camera's readout statistics [37]. A representative histogram of photon counts per camera frame is shown in Fig. 4(d) [Fig. 10], revealing two peaks that correspond to the NV^0 (dark) and NV^- (bright) charge states under orange illumination. The measured charge-state readout fidelity using the camera (88.3%) is similar to that obtained using confocal readout of the same sample (86.3%) with the same objective lens and readout parameters [Fig. 11].

Having achieved multiplexed charge-state measurements using targeted excitation, we then add a spin-selective ionization pulse to implement multiplexed SCC by modulating the power of the orange laser between ionization (approximately 10 mW per spot) and readout (approximately 20 μW per spot). We compare the charge-state readout statistics for a representative NV center spin prepared in either the $m_s = 0$ or $m_s = -1$ spin state to benchmark σ_R [Fig. 4(e)]. The spin readout noise for the data shown in Fig. 4(e) is $\sigma_R \approx 12$, a fourfold improvement over green readout in a confocal microscope [21] and a tenfold improvement over wide-field green readout [Fig. 9]. However, our scheme performs worse than previous implementations of SCC using a red (637 nm) laser for ionization ($\sigma_R \sim 5$) [34], which we attribute to a higher charge-state recombination rate from the orange laser [38], in agreement with a rate equation model [39] [Fig. 13].

To understand the scalability of our multiplexed SCC protocol, we investigate the scaling of σ_R as a function of the number of multiplexed NV centers with a constant total ionization pulse power [Fig. 4(f)]. We observe that σ_R increases as we increase the number of addressed NV centers. We attribute this increase to inefficient charge-state ionization, as the power available for each NV center is reduced when we distribute the fixed total laser power across more NV centers. This indicates that the scale of our multiplexed SCC experiment is limited only by the currently available ionization laser power (30 mW).

IV. MULTIPLEXED COVARIANCE MAGNETOMETRY

Equipped with multiplexed SCC, we demonstrate parallelized covariance magnetometry from simultaneous measurements of NV centers at different locations $\vec{x}_i$ [34]. We target four NV centers [Fig. 5(a)] from which we simultaneously measure $\binom{4}{2} = 6$ two-point correlators. To demonstrate that the measured correlations result from spin dynamics rather than spurious correlations [34], we use a separate green laser to prepare one of the NV centers (NV4)

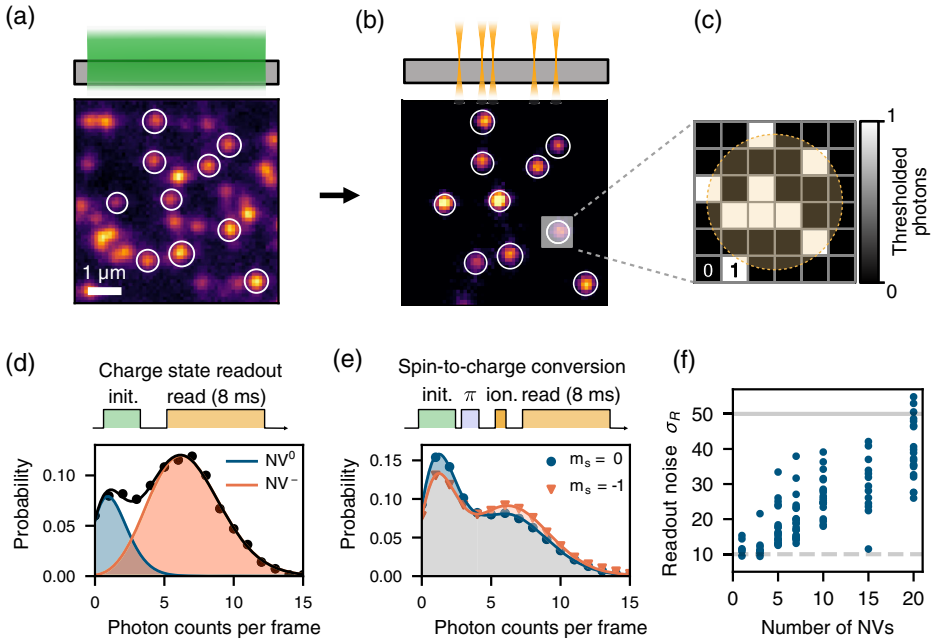


FIG. 4. Multiplexed spin-to-charge-conversion readout using a spatial light modulator. (a) Wide-field imaging using green excitation enables localization of single NV centers, whose coordinates are recorded. (b) The SLM enables selective excitation with the orange laser, enabling ionization and charge-state readout. (c) Diagram of photon counting using the EMCCD camera. In a 6 pixel by 6 pixel region around each NV center (dashed circle), photons are counted by defining a detection threshold for each pixel and summing. (d) Charge-state readout of an NV center using SLM excitation. Top: wide-field green laser pulse initializes the NV center charge state, which is then read out using a weak orange pulse whose duration is matched to the camera exposure (8 ms). The pulse sequence is repeated several thousand times, and the resulting counts per NV center per frame are put in a histogram, with a representative histogram for one NV center shown (bottom). The curves are fits to two Poisson distributions that correspond to the relative populations of NV^0 and NV^-, with charge-state readout fidelity of $88.3 \pm 0.5\%$. (e) Spin-to-charge conversion using the SLM. Top: after green laser initialization, a MW π pulse can be applied to flip the spin from $m_s = 0$ to $m_s = -1$. The orange laser is then amplitude modulated to ionize the NV centers (high power, short pulse) and read out the charge state (low power, long pulse). Bottom: the resulting photon number distributions for the $m_s = 0$ and $m_s = -1$ spin states for a representative NV center when the ionization laser power is distributed over three NV centers are shown. (f) Readout noise σ_R as a function of number of simultaneously measured NV centers. Each point represents the measured σ_R from an NV center. At high numbers, the readout noise is limited by low ionization intensity. At low NV numbers (high ionization power), the readout noise is limited by the recombination of NV^- back to NV^0.

in the opposite spin state from the other three (NV1–3) [Figs. 5(a) and 5(b)]. To verify our ability to detect two-point correlators with our achievable readout noise, we first measure correlations introduced by direct NV spin driving rather than noise sensing [Fig. 5(b)]. This allows us to rapidly drive the NV centers to mitigate the effect of decoherence under free evolution, as well as to circumvent quantum projection noise, as we are able to intentionally drive each NV center between pure states $m_s = 0$ and $m_s = -1$. In this driven-spin correlation experiment, we interleave two pulse sequences: In the even-numbered experiments we simultaneously drive all the NV centers around the Bloch sphere by an angle θ, while in the odd-numbered experiments we drive the NV centers by an angle $\theta + \pi$ [Fig. 5(b)]. At the end of each experiment, we read out a single camera frame, simultaneously measuring the four signals s_i where $i = 1 \ldots 4$ indexes the NV center. Lastly, we use the set of acquired signals across experiments $S_i = \{s_{i,k}\}$, where k indexes the experiment number, to compute the Pearson correlation for each NV pair: $r_{ij} = \mathrm{Cov}(S_i, S_j)/(\sigma_i \sigma_j)$, where Cov is the covariance and σ_i is the standard deviation of S_i. From the computed Pearson correlations, we subtract off a uniform background correlation measured using an independent calibration experiment [Fig. 14]; the resulting correlations are shown in Fig. 5(c). As expected for each pair of NV centers prepared in the same initial spin state (NV1–3), the correlations between the measured signals are maximized when $\theta = n\pi$ for integer n, as the two spins flip synchronously between $m_s = 0$ and -1, and are minimized for $\theta = (n + 1/2)\pi$, since the readout projects the two spins randomly and independently onto $m_s = 0$ or -1. Conversely, each NV center's correlation with NV4 is negative, as NV4 has been prepared in the opposite orientation and, thus, acquires an opposite phase. In addition, the amplitude of the correlation oscillation indicates the maximum measurable correlation, which is $1/\sigma_{R_i}\sigma_{R_j}$. From Fig. 5(c), we estimate $\sigma_{R_i} = 15 \pm 1$,

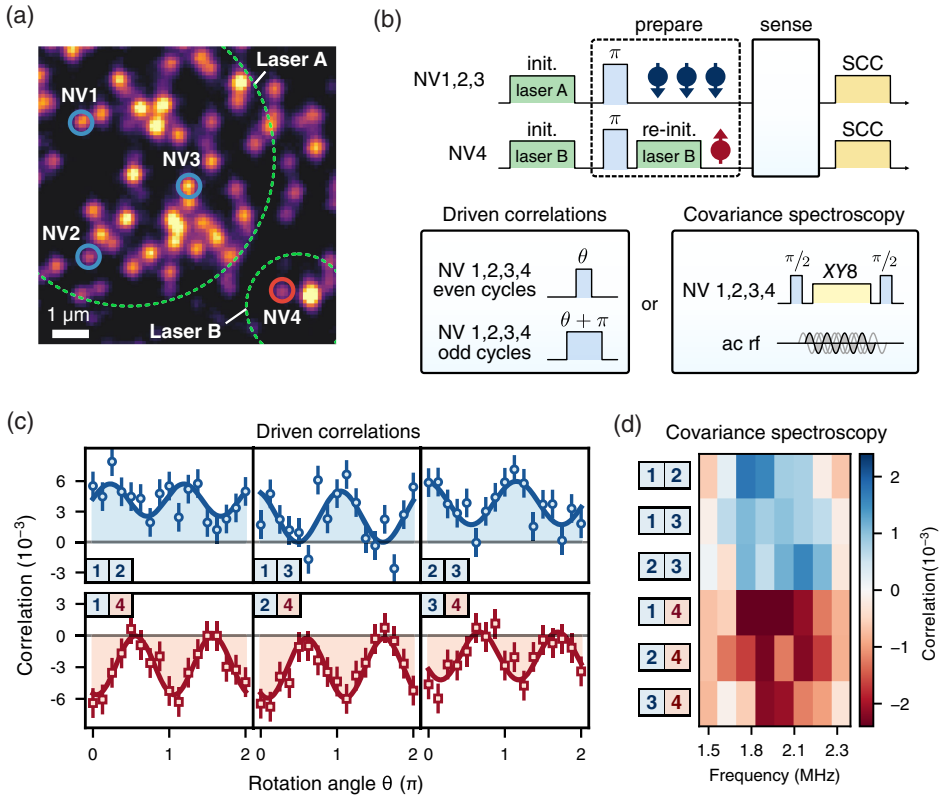


FIG. 5. Multiplexed correlation measurements. (a) Wide-field image showing the four targeted NV centers. The NV center spin and charge states are initialized by lasers A and B, where A addresses NV1–3 and B addresses only NV4, enabling selective reinitialization. (b) Pulse sequences of the two types of correlation experiments carried out. We demonstrate the measurement of driven-spin correlations and spectroscopy of a correlated field using four NV centers. In both experiments, we prepare three NV centers (NV1–3) in the same spin state and one NV center (NV4) in the opposite spin state. In the driven-spin correlation experiment, we interleave MW pulses that rotate the spin by either θ or $\theta + \pi$ and sweep θ. In the spectroscopy experiment, we run an $XY8$ sensing sequence with a fixed interpulse spacing while applying an ac magnetic field to the sample and sweeping the ac frequency. (c) Driven-spin correlations between four NVs as a function of θ. The three blue curves on the top show positive correlations between NV1–3, and the three red curves on the bottom show negative correlations between NV4 and NV1–3. The error bars represent the standard error. (d) Covariance noise spectroscopy of an applied field with four NV centers. The three NV pairs that start in the same spin state show positive correlations, while the three pairs that start in the opposite spin states show negative correlations.

consistent with the data in Fig. 4(c). We also use multiplexed covariance magnetometry to perform covariance noise spectroscopy of an applied ac magnetic field [34]. As before, we prepare NV1–3 in the same spin state and prepare NV4 in the opposite state. We then use an $XY8$ sensing sequence [40] with a fixed interpulse spacing and sweep the frequency of the applied ac signal [Fig. 5(d)]. When the frequency matches the interpulse spacing, NV1–3 show positive pairwise correlations from the correlated phase they accumulate due to the shared noise, and NV4 shows negative pairwise correlations with NV1–3 because of the opposite phase accumulation.

V. RECONSTRUCTION OF NONLOCAL MAGNETIC FIELD CORRELATORS

Multiplexed covariance magnetometry enables simultaneous measurement of Pearson correlations between many NV centers. The measured raw correlations encode spatially correlated magnetic field noise but also depend on each NV center's individual spin state readout noise and coherence time [Eq. (H1)] [34]. In order to learn the intrinsic correlation structure of a target system, we must first deconvolve the NV center sensor statistics.

To this end, we now demonstrate the quantitative reconstruction of noise correlations in a physical system with a known magnetic field profile. We fabricate a current-carrying wire on the diamond surface, apply a noise signal consisting of a phase-random ac current at 2 MHz through the wire, and measure the raw correlations from five NV centers that experience different signs and amplitudes of magnetic noise using an $XY8$ sensing sequence. The measured raw correlations due to current noise [Fig. 6(b), upper right] show the expected qualitative structure of the underlying correlations; NV centers located on opposite sides of the wire are anticorrelated. Quantitatively, the

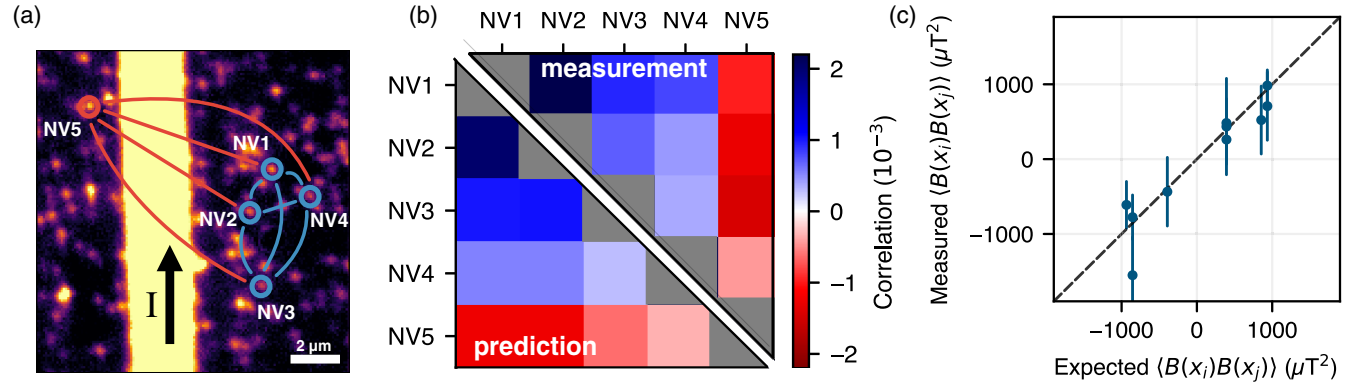


FIG. 6. Reconstructing spatial correlations using multiplexed covariance magnetometry. (a) Wide-field image showing five target NV centers and a current-carrying wire patterned on the diamond surface. Applied current through the wire results in oppositely oriented magnetic field projection normal to the diamond surface on opposite sides. The NV center pairs connected with blue (red) lines are expected to show positive (negative) correlations. (b) Correlation matrix showing the measured (upper-right) and predicted (lower-left) raw correlations between five NV centers. Predicted correlation amplitudes are given by spin readout noise, coherence time, and correlated magnetic noise amplitude. (c) Measured and expected magnetic field noise correlators. By independently measuring σ_R and $T_{2,XY8}$ in the absence of the applied noise signal, the intrinsic magnetic field noise correlators can be calculated from the measured Pearson correlations in (b). The error bars represent the standard deviation.

expected correlations among NV centers will depend on their positions with respect to the wire, which changes the magnitude of the magnetic field that they experience. Each NV center also has different readout noise (σ_R) and coherence time ($T_{2,XY8}$), which changes the magnitude of the observed raw correlations r_{ij} [Eq. (H1)]. Using independent measurements of σ_R and $T_{2,XY8}$ of each NV center without the applied noise signal, we predict the raw correlation amplitudes [Fig. 6(b), lower left], which closely match the measured raw correlations.

The relationship between the Pearson correlation and correlated magnetic noise for small accumulated phases is given by

$$\frac{1}{\pi}\int_0^\infty S_C(\omega)\frac{F(\omega)}{\omega^2}d\omega = \sinh^{-1}\left(r_{ij}\frac{\sigma_{Ri}\sigma_{Rj}}{e^{-\chi_i(t_i)-\chi_j(t_j)}}\right), \quad (1)$$

where $S_C(\omega)$ is the correlated magnetic noise spectral density, $F(\omega)$ is the pulse sequence filter function, and $\chi_i(t_i) = (t_i/T_{2,XY8,i})^p$ is the NV center decoherence function with stretched exponent p. In our experiment, the applied noise signal is a phase-random, monochromatic ac magnetic field at frequency f_{ac}, which we sense using a Carr-Purcell (CP) sensing sequence. Under these conditions, we can derive the intrinsic magnetic noise correlators from Eq. (1):

$$\langle B(x_i)B(x_j)\rangle = \frac{\sinh^{-1}\left(r_{ij}\frac{\sigma_{Ri}\sigma_{Rj}}{e^{-\chi_i(t)-\chi_j(t)}}\right)}{\gamma_e^2 t^2 \bar{W}^2(f_{ac})}, \quad (2)$$

where γ_e is the electron gyromagnetic ratio, t is the total phase accumulation time, and $\bar{W}^2(f_{ac})$ is the pulse sequence weighting function at the noise frequency [41] [Appendix J]. We reconstruct the magnetic noise correlators and compare to the expected values [Fig. 16] based on independent measurements of the local noise amplitude at each NV center [Fig. 6(c)]. We find excellent agreement between the expected and reconstructed correlator amplitudes, demonstrating the ability to quantitatively determine spatially correlated magnetic field structure from multiplexed covariance magnetometry measurements.

VI. OUTLOOK

The platform demonstrated here can be readily extended to accomplish low readout noise measurements of many more NV centers. Provided 10 W of ionization laser power, we could address 500 NV centers resulting in more than 10^5 measured two-point correlators. The multiplexed readout demonstrated here is essential to measuring higher order joint cumulants, which is a promising direction for future studies. Additionally, while we demonstrated only multiplexed spatial correlation measurements, we could readily extend this platform to measuring temporal correlations. Measuring temporal correlations requires independent microwave control in addition to the global optical initialization and readout [34], which could be accomplished by addressing NV centers of different orientations that are spectrally separated. Moreover, performing ionization at a more optimal wavelength is expected to reduce σ_R further. Finally, extending these techniques to measure correlations below the diffraction limit [42] would allow for the measurement of many two-point correlators with nanometer separations simultaneously.

Our platform opens the door to high-throughput measurements of magnetic fields across large areas with

nanoscale localization, with immediate applications in magnetometry of condensed matter dynamics. Just as scanning NV magnetometry has advanced our understanding of magnetic ordering [43], transport [44–46], and superconductivity [47,48] through high-resolution imaging of magnetic fields, our platform will provide a new window into dynamics through wide-field mapping of local noise spectra and nonlocal correlation functions at many length scales simultaneously. Specifically, local noise measurements can provide a quantitative probe of dynamics [49,50], for instance, in measuring critical exponents of phase transitions in 2D antiferromagnets that have vanishing stray fields [24,28]. Additionally, access to nonlocal correlation functions with nanoscale precision will enable study of the dynamics in systems that are fundamentally characterized by correlations, such as in hydrodynamic electron flow [27,51,52], magnetic 2D materials [24,28], vortex dynamics in superconductors [53,54], and spin liquids [30,55].

Note added. We are aware of a manuscript [56] that describes complementary work to perform multiplexed measurements with NV centers in diamond. Both works deploy low-noise cameras to measure many NV centers simultaneously; in Ref. [56], Cambria, Chand, and Kolkowitz employ a complementary approach for initialization and ionization by using an acousto-optic deflector instead of an SLM to achieve high optical power density.

ACKNOWLEDGMENTS

We gratefully acknowledge helpful conversations with Pai Peng, Artur Lozovoi, Matthew Cambria, and Shimon Kolkowitz. This work was supported by the Gordon and Betty Moore Foundation (GBMF12237, DOI 10.37807), the National Science Foundation (Grant No. OMA-2326767), and the Intelligence Community Postdoctoral Research Fellowship Program by the Oak Ridge Institute for Science and Education (ORISE) through an interagency agreement between the U.S. Department of Energy and the Office of the Director of National Intelligence (ODNI) (J. R. and Z. K.).

K.-H. C., J. R., and N. P. d. L. conceived the experiment platform. K.-H. C. and Z. K. built the optical setup with inputs from J. R., B. Z., and L. S. N. K.-H. C. wrote the control software. B. Z. and J. D. T. instructed the setup of the spatial light modulator. K.-H. C. and Z. K. collected and analyzed the data. K.-H. C. performed the numerical simulation and derivations. J. D. T. and N. P. d. L. supervised the project. K.-H. C., Z. K., J. R., and N. P. d. L. wrote the manuscript with input from all the authors.

The authors declare no competing financial interests.

DATA AVAILABILITY

The data that support the findings of this study are available from the corresponding author upon reasonable request.

APPENDIX A: EXPERIMENTAL DETAILS

The 5×5 mm diamond sample was implanted with a nitrogen ion energy of 3 keV, vacuum annealed to form NV centers, and then oxygen annealed [18], resulting in shallow NV centers within approximately 10 nm of the surface. NV center measurements are performed in a home-built setup that include a wide-field illumination path, an SLM excitation branch, and an imaging path. The sample is mounted in a closed-cycle cryostat (Montana Instrument S100), optically interfaced through a Zeiss 100×, NA = 0.9 objective. All experiments were done at room temperature. We built this platform around a cryostat so that it is immediately compatible with cryogenic conditions without modification to the experimental setup. The wide-field green laser used for imaging of the NV centers and wide-field spin measurements is provided by a 532 nm diode-pumped solid state laser (Coherent Genesis STM CX-5000), modulated by an acousto-optic modulator (AOM) (Isomet M1205-P80L-1) in a double-pass configuration. The orange laser used for SCC as well as NV center charge-state readout is a 594 nm, diode-pumped solid state laser (Hubner Cobolt Mambo) equipped with an internal AOM for both digital and analog modulation of the laser power. The two excitation lasers are combined by a dichroic mirror (Semrock AF567-Di01). The laser powers (as measured before the objective lens) used were approximately 15 μW per NV center for charge-state readout, approximately 30 mW in total for the ionization pulse of SCC (equally distributed across all the NV centers being addressed), and approximately 50 mW for green wide-field imaging and charge-state initialization. Both excitation lasers are circularly polarized before the objective (Thorlabs WPQ10M-532 and WPQ10M-588). The local reinitialization laser for demonstrating anticorrelations in covariance magnetometry is a 520 nm diode-pumped solid state laser (Hubner Cobolt MLD-06).

The readout path is separated from the excitation by a dichroic mirror (Semrock FF647-SDi01). The NV center fluorescence is filtered to have a pass band of 650–800 nm and then imaged onto an EMCCD camera (Nuvu HNu-512). All the experiments were done with an EM gain of 5000. For the wide-field spin experiments, the camera is exposed to the NV center fluorescence for multiple iterations and read out periodically. The length for each exposure is chosen empirically based on the optical intensity of the excitation laser and the laser duty cycle to prevent the camera from being overexposed. The data shown in Fig. 3 are obtained this way.

An SLM (Santec SLM-210) is used to generate a laser pattern on the diamond sample to selectively address the NV centers chosen for SCC readout. We incorporate an open-source SLM control software package [57] for SLM calibration and phase pattern generation. The laser pattern is sampled from the main optical path onto a CMOS camera (Thorlabs CS165MU) for adaptive pattern calibration. The SLM pattern that corresponds to the locations of the selected NV centers is generated after selecting the NV positions, as shown in Fig. 1(a).

Microwave pulses are generated using a Rohde and Schwarz signal generator (SMATE200A), amplified (Mini-Circuits ZHL-16W-43S+), and sent to a homemade microwave printed circuit board. IQ phase modulation is achieved using an arbitrary waveform generator (AWG) (Keysight 33622A) that modulates the signal generator. The low-frequency ac test signal around 2 MHz is generated with another AWG (Keysight 33622A) and amplified (Mini-Circuits LZY-22+). The global noise signal in Fig. 5(d) was delivered to the sample via a copper coil loop fixed around the diamond sample. The current-carrying device in Fig. 6 was deposited directly on the diamond surface and lithographically defined.

APPENDIX B: WIDE-FIELD SPIN MEASUREMENTS OF MANY NV CENTERS

Conventional confocal microscope NV center measurements use single-photon avalanche photodiodes that have nanosecond timing resolution and submicrosecond readout rate. In the conventional experiment configuration, it is possible to read out each 300 ns shot of NV center experiments, which typically have repetition rates on the order of 10 kHz to MHz. However, in the wide-field case, since the EMCCD frame rate is less than 100 Hz when operating in the full frame, it is impractical to operate the camera the same way as we would for conventional NV experiments. To overcome this issue, instead of reading out every experiment shot separately, we integrate the fluorescence from multiple pulsed experiments on the EMCCD and then read out the frame after a certain number of repetitions before saturating the camera. We take a reference frame using the same approach with the same camera exposure time and laser duty cycle but without applying the MW pulse(s). The schematics of a pulse diagram is shown in Fig. 3(b). This approach allows us to implement multiplexed pulsed microwave experiments using the camera, shown in Figs. 3(a) and 3(c).

The fluorescence signal for each NV center is obtained through the following process. First, the locations of NV centers are determined from a wide-field image by running a blob-detection algorithm. After the locations of the NV centers are determined, we sum the pixel values in an $n \times n$ region centered around each NV center for both signal and reference frames to obtain the signal count c_{sig} and reference count c_{ref}. That is,

$$c_{\mathrm{sig,ref}} = \sum_{i=1}^{n}\sum_{j=1}^{n} c^{\mathrm{raw}}_{\mathrm{sig,ref}}(i,j), \tag{B1}$$

where c^{raw} denotes the raw camera reading. In this work, we choose $n = 6$ based on the size of NV center image on the EMCCD. The normalized fluorescence is obtained by dividing c_{sig} by c_{ref}, i.e., $c_{\mathrm{norm}} = c_{\mathrm{sig}}/c_{\mathrm{ref}}$, to cancel out slow drifts in fluorescence intensity over time. With this data acquisition approach tailored to measuring a single NV center with the conventional green readout on an EMCCD, we measure the cw ODMR spectra of the NV centers [Fig. 1(d)], fit the spectra, and run Rabi oscillation on our selected resonance frequency using the aforementioned pulsed experiment method to calibrate our π-pulse time for subsequent pulsed experiments.

We calculate the dc magnetic field sensitivity of the NV centers from the ODMR spectrum using

$$\eta \approx \frac{h}{g\mu_B}\frac{\Delta\nu}{C\sqrt{\mathcal{I}_0}}, \tag{B2}$$

where $g \approx 2$ is the Landé g factor, μ_B is the Bohr magneton, $\Delta\nu$ is the ODMR linewidth, C is the ODMR contrast, and $\mathcal{I}_0$ is the fluorescence detection rate [1]. We fit each individual ODMR spectrum to obtain the linewidth $\Delta\nu$ and the contrast C and obtain the fluorescence rate $\mathcal{I}_0$ for each NV center from the wide-field image. The resulting dc magnetic field sensitivity map is shown in Fig. 2(c). Note that more than 60% of the NV centers have a sensitivity less than 30 $\mu\mathrm{T\,Hz^{-1/2}}$, comparable to the sensitivity obtained from a single NV center measured with a confocal microscope [Fig. 8]. The histogram of the dc magnetic field sensitivity from the wide-field dataset is shown in Fig. 7.

In addition, we benchmark the spin readout noise, σ_{R} using wide-field green excitation. σ_{R} is defined as

$$\sigma_{\mathrm{R}} = \sqrt{1 + 2\frac{\sigma_0^2 + \sigma_1^2}{(\alpha_0 - \alpha_1)^2}}, \tag{B3}$$

where $\sigma^2_{0,1}$ and $\alpha_{0,1}$ are the variances and means, respectively, of the $m_s = 0$, 1 state photon number distributions [34]. The σ_{R} of most NV centers are above 100, which is several times to an order of magnitude worse than the green readout using a confocal microscope [Fig. 9]. We attribute the high readout noise to the following three causes: (i) The EMCCD, unlike confocal microscopes, does not have a pinhole in the detection optical path to block out-of-plane light, so the EMCCD readout suffers from increased background fluorescence. (ii) The spin contrast we obtain from the EMCCD using the protocol described above is lower than that obtained from a confocal microscope, because, when we integrate multiple pulsed experiments on one EMCCD exposure, we collect the fluorescence while the NV center spin is reinitialized, reducing the spin

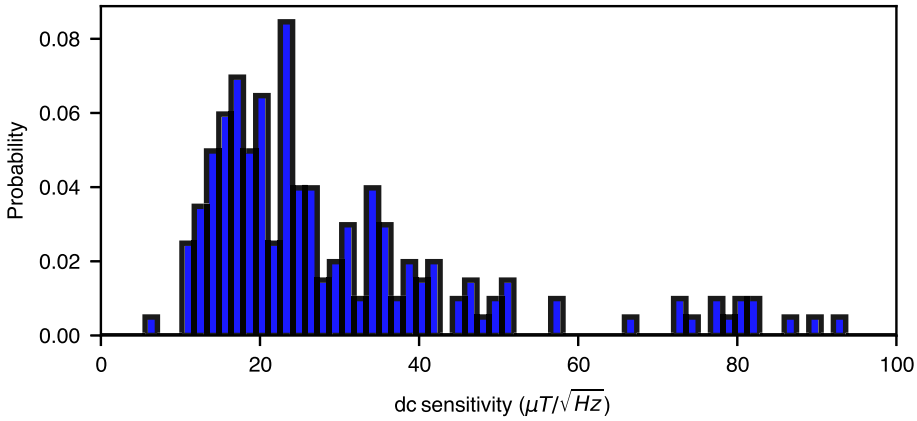


FIG. 7. Histogram of dc magnetic field sensitivity. Histogram of the dc magnetic field sensitivity of the NV centers in Fig. 2(c). Over 60% of the NV centers have sensitivities between 10 and 30 $\mu T\,Hz^{-1/2}$.

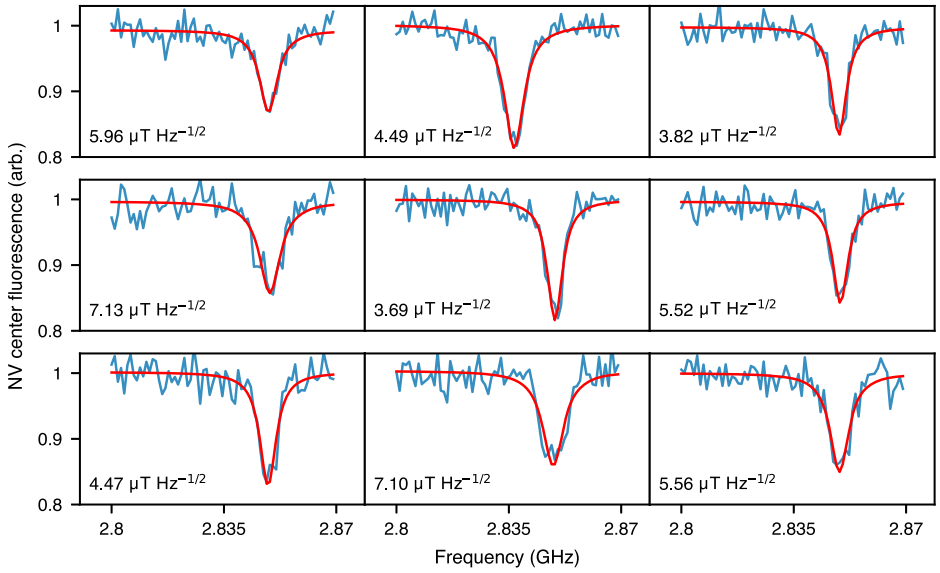


FIG. 8. dc magnetic field sensitivity measured with a confocal microscope setup. cw ODMR spectra are measured for 9 NV centers in the same sample using a confocal microscope setup. The corresponding dc magnetic field sensitivities are labeled for each curve.

contrast. (iii) The optical power density we use is approximately 2 orders of magnitude lower than the saturation power of a single NV center in a confocal microscope setup.

APPENDIX C: MULTIPLEXED NV CENTER CHARGE-STATE READOUT

To read out the NV center charge state, the NV centers are first imaged using the wide-field green laser, and then the positions of the selected NV centers are determined from the image by fitting the image to a 2D-Gaussian distribution.

The fitted NV coordinates can then be used to generate the required phase pattern on the SLM using a w-GS algorithm. During readout, the image is processed in real time to extract the photon counts from each NV center. The photon number for a given NV center in a given readout, S, is obtained by integrating an $n \times n$ region around the target NV center. That is,

$$S = \sum_{i=1}^{n} \sum_{j=1}^{n} c(i,j), \tag{C1}$$

where $c(i,j)$ is the photon count at pixel (i,j). In this work, we choose $n = 6$ based on the image size of an NV center. To obtain the photon count at each pixel, the pixels are thresholded to determine whether they detected either zero or one photon based on the raw camera readings. That is,

$$c(i,j) = \begin{cases} 0, & \text{if } c_{\text{raw}}(i,j) \le t_{\text{pc}}, \\ 1, & \text{if } c_{\text{raw}}(i,j) > t_{\text{pc}}, \end{cases} \tag{C2}$$

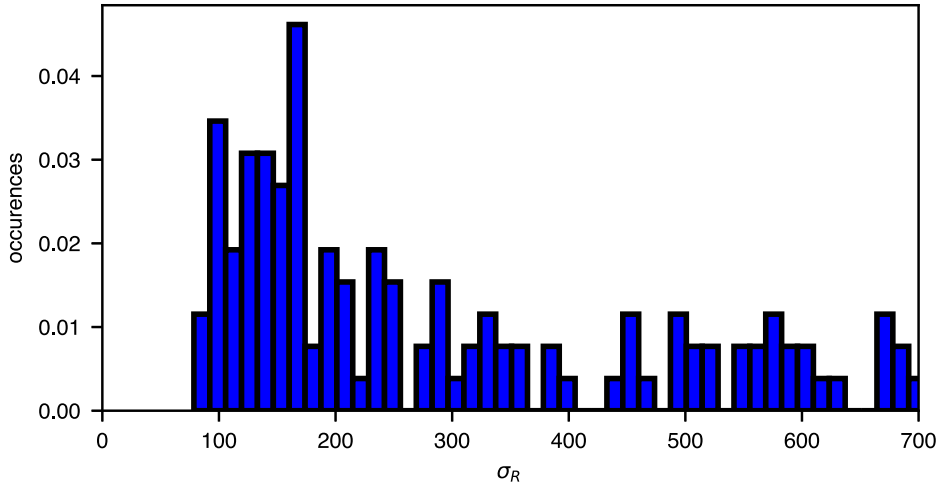


FIG. 9. Histogram of spin readout noise using multiplexed wide-field green readout. The spin readout noise of most measured NV centers is well above 100, which is several times worse than that achieved by green readout using a confocal microscope. The increase in readout noise can be attributed to (i) increased background fluorescence for camera readout, (ii) lower spin contrast since the camera is always exposing during a pulsed experiment, and (iii) low optical power density.

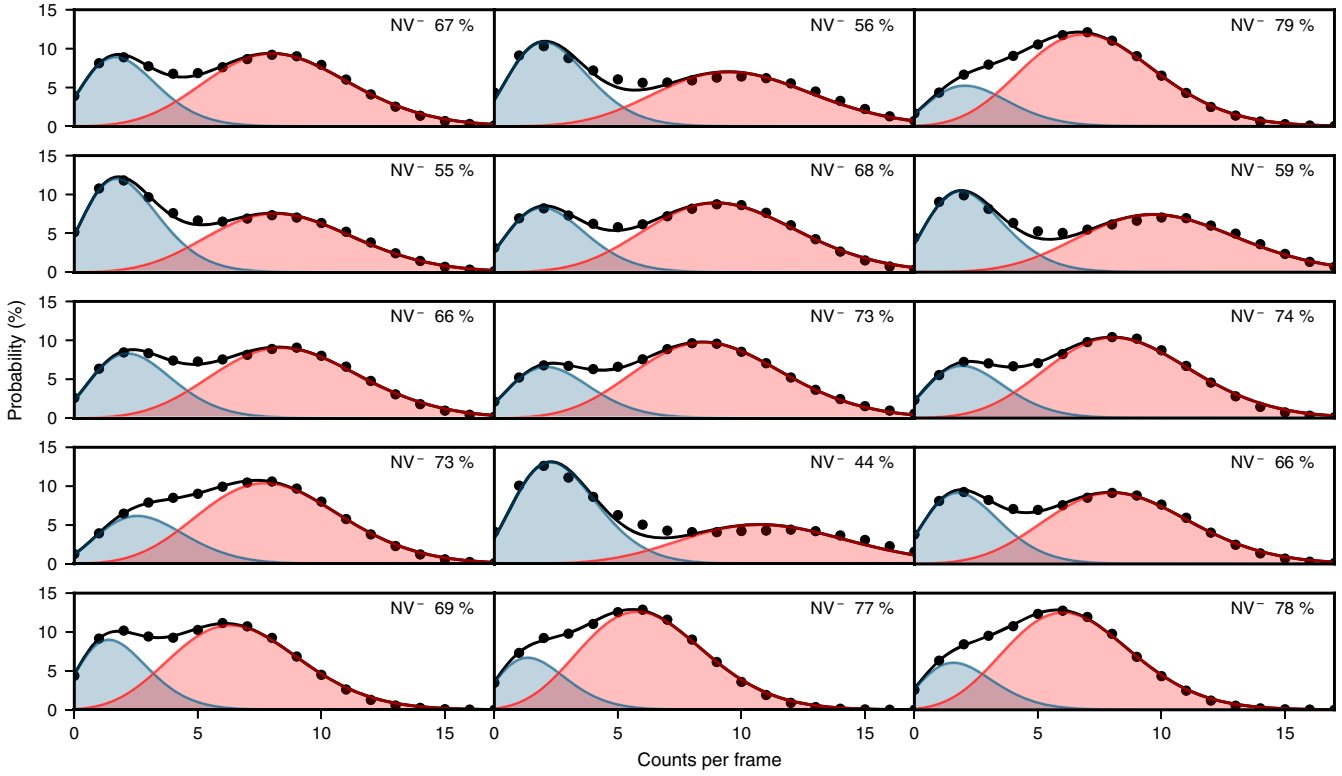


FIG. 10. Multiplexed charge-state readout on 15 NV centers. 15 NV centers are targeted with the SLM, and the charge states are read out simultaneously using the EMCCD. The photon counts per shot of individual NV centers are recorded at each experiment iteration and put into a histogram. The curves are fits to double-Poisson distributions, where the two colors indicate the NV^0 (blue) and NV^- (red). The steady state NV^- population of the NV centers is extracted from the relative area under the fit curves of the two Poisson distributions.

where $c_{\mathrm{raw}}(i,j)$ is the raw camera reading for pixel (i,j) and t_{pc} is the photon counting threshold. During readout, the selected NV centers are illuminated with focused orange laser beams, and their fluorescence is collected on the EMCCD during the camera exposure. The photon-detection threshold must be large enough to surpass the readout noise of the EMCCD readout circuit. We do not observe a strong effect on both charge-state population and

spin readout noise when we sweep the photon-detection threshold (t_{pc}) around the chosen value. The thresholded photon counts in each NV region are then summed to yield the final counts per NV center per frame. The photon counts in Figs. 4 and 10 are obtained in this way. As a demonstration that we are able to read out the charge state of multiple NV centers in parallel, the simultaneous charge-state readout histograms of 15 NV centers are plotted in Fig. 10. From the double-Poisson fit to the histogram, we extract the relative charge-state populations. We attribute the low NV^- population of some NV centers to surface inhomogeneities that destabilize the charge state of the near-surface NV centers.

APPENDIX D: SENSITIVITY AND CHARGE-STATE READOUT FIDELITY COMPARISON TO CONFOCAL MICROSCOPE MEASUREMENT

To benchmark the dc magnetic field sensitivity and charge-state readout fidelity of the multiplexing experiments against conventional confocal measurements, we perform cw ODMR and charge-state readout using confocal excitation and collection with the same diamond sample and objective lens. The resulting cw ODMR spectra and the corresponding dc magnetic field sensitivities are presented in Fig. 8, indicating that our wide-field sensitivity is within an order of magnitude of that measured with a confocal microscope. We attribute the discrepancy between sensitivities measured with camera and confocal readout to the lower spin state readout contrast using the camera, as described in previous sections.

A typical NV center charge-state readout histogram using a confocal microscope with the same readout time as that of the histogram in Fig. 4(d) is shown in Fig. 11. The associated charge-state readout fidelity is $86.3 \pm 0.8\%$, a typical value with these readout parameters, indicating that the charge-state readout fidelity on the camera [$88.3 \pm 0.5\%$ in Fig. 4(d)] is comparable to that obtained from a confocal microscope measurement.

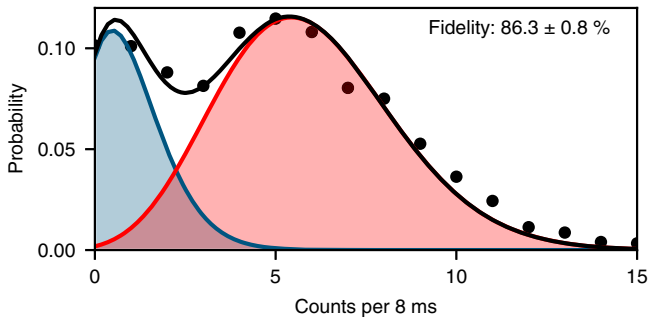


FIG. 11. Charge-state readout using a confocal microscope setup. A typical NV center charge-state readout histogram using a confocal microscope is shown. The charge-state readout fidelity is $86.3 \pm 0.8\%$. The optical setup, the diamond sample, and readout time are the same as the ones in Fig. 4(d). The curves are double Poisson fit to the histogram.

APPENDIX E: MULTIPLEXED SPIN READOUT NOISE MEASUREMENT

A key parameter for covariance magnetometry sensitivity is the spin-state readout noise σ_R. We use the SLM to implement SCC on multiple NV centers and benchmark the efficacy of the scheme by measuring the spin-dependent photon statistics for the $m_s = 0$ and $m_s = -1$ spin states to obtain σ_R. Note that, in order to use the same laser for both ionization and readout, we modulate the control voltage of the AOM after calibrating the input voltage and output power. To measure the photon statistics for the $m_s = 0$ state, we initialize the NV center spin state and charge state and implement SCC readout. For the $m_s = -1$ state, we apply a MW π pulse after initialization and read out using SCC. Figure 4(e) shows an example of the histograms of the photon counts for the two spin states for a single NV center. We then extract the statistics of the two distributions to compute σ_R using Eq. (B3).

Since the efficacy of SCC depends on both the ionization step that maps different spin states into different charge states and the readout step, σ_R is a function of four parameters: ionization power, ionization time, readout

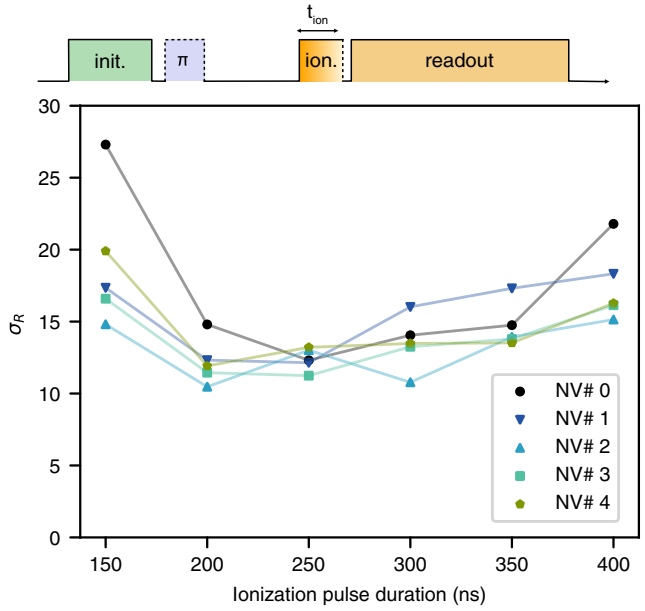


FIG. 12. Optimizing parameters for multiplexed SCC. We measure the spin readout noise σ_R of five NV centers simultaneously by comparing the readout photon statistics for each NV centers in the $m_s = 0$ (no π pulse) and $m_s = -1$ (π pulse) after the SCC process. To optimize the readout noise as described in the main text, we sweep the ionization pulse time to minimize the readout noise, which is critical for multiplexed covariance magnetometry. In this case, t_{ion} of 250 ns is considered optimal for all the NV centers.

power, and readout time. Therefore, to optimize σ_R, we optimize these four parameters within the constraints of our experiment setup. The readout power and time are set by the sweeping these parameters and measuring the charge-state populations of multiple NV centers [Fig. 10]. We use approximately $10-20$ μW per NV center with a 5 ms readout, because these parameters result in a high-fidelity charge-state readout with reasonable experiment repetition rates. We also observe that small changes in the readout parameters have low effect on the measured σ_R. Since the ionization step is power limited, we fix the ionization power to the maximum available (approximately 30 mW). Therefore, to optimize σ_R, we set readout time, readout power, and total ionization power as detailed above and sweep ionization time, shown in Fig. 12 for five NV centers simultaneously. In this case, the minimum σ_R for all five NV centers is achieved for ionization pulse time around 250 ns.

APPENDIX F: LIMITS TO MULTIPLEXED READOUT NOISE

The minimum σ_R we have measured with our modified SCC scheme is approximately 2–3 times higher than observed in other works [34,35]. By applying a rate equation model [19,39], we study the dependence of σ_R on ionization laser power and wavelength. In our simulation, we assume the following parameters of the NV

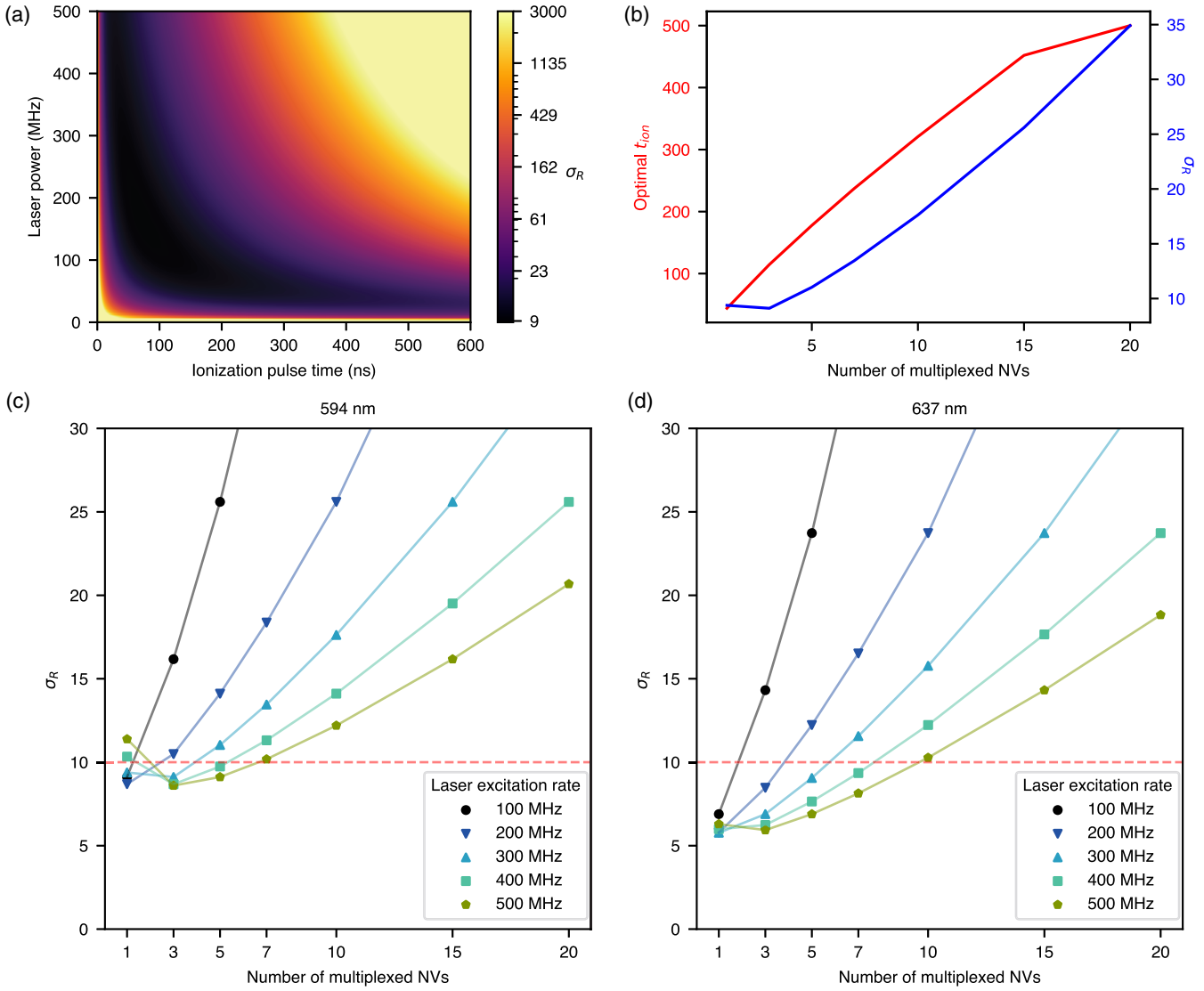


FIG. 13. Effect of ionization laser power, time, and wavelength on spin state readout noise σ_R. (a) σ_R as a function of orange ionization laser power and pulse time simulated using a rate equation model. (b) σ_R and the optimal ionization pulse duration at a laser power that matches our experiment as a function of the number of multiplexed NV centers (inversely proportional to the power per NV center). (c),(d) σ_R as a function of the number of multiplexed NV centers for different total laser power for an orange ionization laser (c) and a red ionization laser (d).

center initial state: 70% NV^- population, 95% initialization into $m_s = 0$ state, and 1.6/6.7 photons on average for the NV^0/NV^- charge-state readout, based on typical results of our charge-state measurements. We evolve the system under the rate equation model with 95% $m_s = 0$ or $m_s = 1$ initial population that correspond to the cases where we apply no MW pulse or a π pulse. At each time step, we extract the photon statistics of both cases from their instantaneous charge-state distribution, $f_0(t)$ and $f_\pi(t)$:

$$f_0(t) = \text{Poisson}(\lambda = \lambda_0) \times p_0^{\text{NV}^0}(t) + \text{Poisson}(\lambda = \lambda_1) \times p_0^{\text{NV}^-}(t), \tag{F1}$$

$$f_\pi(t) = \text{Poisson}(\lambda = \lambda_0) \times p_\pi^{\text{NV}^0}(t) + \text{Poisson}(\lambda = \lambda_1) \times p_\pi^{\text{NV}^-}(t), \tag{F2}$$

where $\text{Poisson}(\lambda)$ is the Poisson distribution with mean λ and $p_{0,\pi}^{\text{NV}^{0,-}}$ denotes the NV center charge-state population for either the neutral (0) or negative (−) charge state with the initial condition of applying a π pulse (π) or not (0). As mentioned above, we assume $\lambda_0 = 1.6$ and $\lambda_1 = 6.7$ for the simulation. From the two photon readout distribution, we can then compute the corresponding statistics to extract the readout noise σ_R with Eq. (B3) to obtain $\sigma_R(t_{\text{ion}})$, where t_{ion} is the evolution time that corresponds to the duration of the ionization pulse [Fig. 13(a)]. The model shows that for a given excitation laser power, as we increase the number of NV centers that we multiplex on (decrease the ionization power per NV center), the optimal ionization pulse time required to obtain the lowest readout noise at a given power increases [Fig. 13(b)], which was also observed qualitatively in experiment. Using the same approach, we investigate the scaling of σ_R as a function of number of multiplexed NV centers for different total available laser power [Fig. 13(c)]. With a lower total available laser power, σ_R increases monotonically as the number of multiplexed NV centers increases. With a higher total power, σ_R first decreases and then increases as the number of multiplexed NV centers increases. The scaling can be understood from the physical process behind SCC, where both too high or too low laser power decreases the ionization contrast between the $m_s = 0$ and $m_s = \pm 1$ states. We also investigate the effect of the ionization laser wavelength on σ_R, which primarily determines the recombination rate from NV^0 back to NV^- [38], and obtain a lower floor for σ_R when using a longer wavelength for ionization [Fig. 13(d)].

APPENDIX G: EFFECTS OF BACKGROUND CORRELATION

In this section, we model and investigate the effect of background correlations on our measurement. We find that the background correlation acts as a constant shift in the baseline correlation, which allows us to subtract off the baseline from our measured correlation data.

We assume two Poissonian sources with mean value μ: $X_1 \sim \text{Poisson}(\mu), X_2 \sim \text{Poisson}(\mu)$ that correspond to signals from two NV centers and assume that the signal strength is randomly modulated by a common Gaussian noise source, $N \sim \text{Normal}(1, \sigma_N)$. This global noise source models the effect of laser power fluctuations and small drifts of the sample between our SLM coordinate calibrations. For simplicity, we assume that both NV centers have the same mean brightness, which holds true for NV centers of the same orientation under the same optical readout power, and define σ_N as the strength of the random fluctuation in our detection process. Thus, the detected signal is $S_i = NX_i$, and the correlation between S_1 and S_2, assuming independent NV centers, is

$$\text{Corr}(S_1, S_2) = \frac{\mu^2\sigma_N^2}{\mu^2\sigma_N^2 + \mu\sigma_N^2 + \mu} \approx \mu\sigma_N^2. \tag{G1}$$

The approximation in Eq. (G1) holds when $\mu\sigma_N^2, \sigma_N^2 \ll 1$, which is a realistic assumption for our experiment.

Now consider the case when the two NV centers are correlated, with a correlation $\text{Corr}(X_1, X_2) = r$. The random fluctuation in readout is still assumed to be independent of the NV signal. In this case, we obtain

$$\text{Corr}(S_1, S_2) = \frac{\mu^2\sigma_N^2 + \mu r(\sigma_N^2 + 1)}{\mu^2\sigma_N^2 + \mu\sigma_N^2 + \mu} \approx \mu\sigma_N^2 + r(\sigma_N^2 + 1). \tag{G2}$$

The difference between the measured correlation, $\text{Corr}(S_1, S_2)$, and the real correlation between the emitters, r, can be computed straightforwardly:

$$\Delta r = \text{Corr}(S_1, S_2) - r = \frac{(1-r)\mu^2\sigma_N^2}{\mu^2\sigma_N^2 + \mu\sigma_N^2 + \mu} \approx (1-r)\mu\sigma_N^2 \geq 0. \tag{G3}$$

The approximation in Eq. (G3) is valid when $\mu\sigma_N^2, \sigma_N^2 \ll 1$. Note that in our case, based on the readout noise we measure, the maximum correlation in NV signal that we should expect from sensing an ac magnetic field signal would be less than 0.5%. Therefore, we may simply assume $\Delta r \approx \mu\sigma_N^2$, indicating that the effect of the background correlation is to add the same constant offset to the real correlation between the NV centers no matter whether the two NV centers are correlated or not. The expressions in Eqs. (G2) and (G3) do not assume a sign for r, which means that, for two emitters that are either positively or negatively correlated, the effect of the background correlation is adding a constant positive offset regardless of the sign of the correlation. Moreover, a more involved analysis for arbitrary initial photon distributions with mean μ and

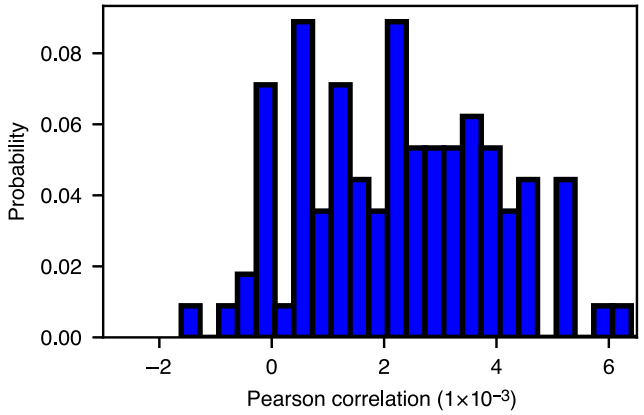


FIG. 14. Background correlation data measured on 15 NV centers simultaneously. We benchmark the magnitude of background correlations by performing multiplexed charge-state readout on 15 NV centers 300 000 times and then computing all pairwise correlations. The mean of the background correlation distribution is approximately 2×10^{-3}, and we subtract this background from all of the covariance magnetometry measurements shown in Figs. 5 and 6.

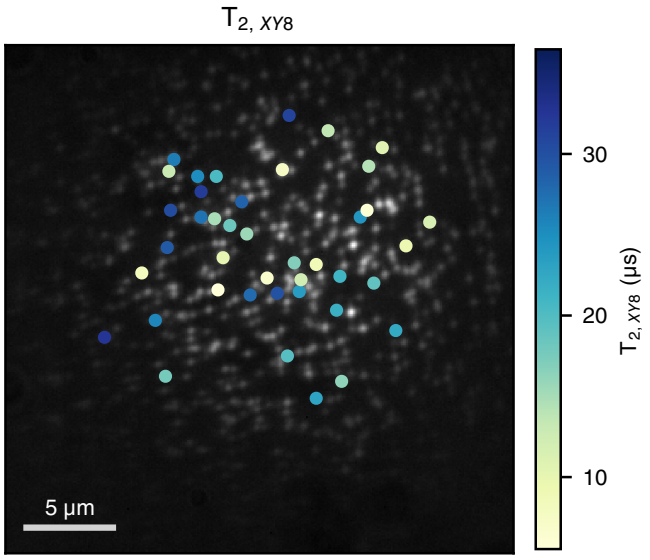


FIG. 15. Wide-field spin coherence time map with $XY8$ dynamical decoupling sequence. We measure the coherence time $T_{2,XY8}$ for the NV centers of the chosen crystallographic orientation before executing the covariance spectroscopy experiment.

variance σ^2 yields the same conclusion as the above analysis.

We measure the background correlation independently of the correlation experiment that we run to obtain an independent baseline. We read out 15 NV centers simultaneously for 300 000 iterations and compute the resulting pairwise correlations, shown in Fig. 14. The mean of the measured background correlation is 2.01×10^{-3}, which we use as our baseline that we subtract off from the measured raw correlation to give the data in Figs. 5(c) and 5(d).

APPENDIX H: CHARACTERIZATION OF THE NV CENTERS FOR MULTIPLEXED COVARIANCE MAGNETOMETRY

The Pearson correlation between NV_i and NV_j is a function of both the NV readout noise and coherence and is given by

$$r_{ij} = \frac{e^{-\chi_i(t_i)-\chi_j(t_j)}}{\sigma_{Ri}\sigma_{Rj}} \langle \sin[\phi_{C_i}(t_i)] \sin[\phi_{C_j}(t_j)] \rangle, \tag{H1}$$

where $\chi_i(t_i) = -(t_i/T_{2,XY8,i})^p$ is the decoherence function and ϕ_{C_i} is the phase accumulated by NV center i due to a correlated field [34]. Since we are working with shallow, near-surface NV centers whose coherence and charge-state stability could be corrupted by surface inhomogeneities, we characterize the NV properties before executing the multiplexed covariance experiment. To understand the coherence of the NV centers, we first run a wide-field $XY8$ dynamical decoupling sequence and sweep the interpulse spacing τ to characterize the NV coherence time $T_{2,XY8}$. The resulting $T_{2,XY8}$ map is shown in Fig. 15. The wide-field $T_{2,XY8}$ data show that the majority of the measured NV centers have coherence time over 15 μs, indicating that for the interpulse spacing $\tau = 250$ ns used in our covariance magnetometry sensing sequence, the decoherence factor in correlation is approximately 0.9^2. Therefore, in the experiment, we pick NV centers that have coherence time greater than 15 μs. As for readout noise, the numbers that we measure from the selected NV centers for the multiplexed covariance magnetometry experiments are consistently around $\sigma_R \approx 12$–15 with minor fluctuations possibly due to the regeneration of laser spot pattern.

APPENDIX I: RELATIONSHIP BETWEEN CORRELATED MAGNETIC NOISE AND PEARSON CORRELATION

Equation (2) gives the magnetic noise correlator between two NV centers that experience phase-random monochromatic correlated noise. To derive the expression, we first consider the phase term in Eq. (H1), $\langle \sin(\phi_1) \sin(\phi_2) \rangle$, where ϕ_1 and ϕ_2 are the correlated phases accumulated by the two NV centers. From there, we have

$$\langle \sin(\phi_1) \sin(\phi_2) \rangle = \frac{1}{2} [\langle \cos(\phi_1 - \phi_2) \rangle - \langle \cos(\phi_1 + \phi_2) \rangle]. \tag{I1}$$

For small accumulated phases with zero mean, we have $\langle \cos(\phi) \rangle = e^{-\langle \phi^2 \rangle/2}$ and find

$$\langle \sin(\phi_1)\sin(\phi_2)\rangle = \sinh(\langle \phi_1\phi_2\rangle)e^{-[\chi_{C1}(t)+\chi_{C2}(t)]}, \quad \text{(I2)}$$

where $\chi_{Ci}(t)$ denote the decoherence functions resulting from the correlated noise [41].

Generically, the term $\langle \phi_1\phi_2\rangle$ can be written as

$$\langle \phi_1\phi_2\rangle = \frac{1}{\pi}\int_0^\infty S_C(\omega)\frac{F(\omega)}{\omega^2}d\omega, \quad \text{(I3)}$$

where $S_C(\omega)$ is the noise spectral density of the correlated field and $F(\omega)$ is the pulse sequence filter function [41]. Then, for arbitrary noise spectral density, we find the relationship of Pearson correlation to measured magnetic noise by substituting Eq. (H1) into Eq. (I3):

$$\frac{1}{\pi}\int_0^\infty S_C(\omega)\frac{F(\omega)}{\omega^2}d\omega = \sinh^{-1}\left(r_{ij}\frac{\sigma_{Ri}\sigma_{Rj}}{e^{-\chi_i(t_i)-\chi_j(t_j)}}\right), \quad \text{(I4)}$$

where $\chi_i(t_i)$ is the total decoherence function. This relates the correlated magnetic noise to measured Pearson correlations, spin readout noise, and decoherence.

Finally, since we are sensing phase-random monochromatic ac magnetic noise at frequency $f_{\rm ac}$, using a *CP*-type pulse sequence, we can explicitly use a relationship between $\langle \phi_1\phi_2\rangle$ and $\langle B(x_1)B(x_2)\rangle$ given by [41]

$$\langle \phi_1\phi_2\rangle = \gamma_e^2\langle B(x_1)B(x_2)\rangle t^2\bar{W}^2(f_{\rm ac}), \quad \text{(I5)}$$

where t is the total phase accumulation time and $\bar{W}^2(f_{\rm ac}) = \{[\sin^2(\pi f_{\rm ac}n\tau)]/[2(\pi f_{\rm ac}n\tau)^2]\}[1-\sec(\pi f_{\rm ac}\tau)]^2$ is the pulse sequence weighting function at the noise frequency [41]. Thus, we obtain

$$\langle B(x_i)B(x_j)\rangle = \frac{\sinh^{-1}\left(r_{ij}\frac{\sigma_{Ri}\sigma_{Rj}}{e^{-\chi_i(t)-\chi_j(t)}}\right)}{\gamma_e^2 t^2\bar{W}^2(f_{\rm ac})}, \quad \text{(I6)}$$

where $\chi_i(t)$ is the decoherence function resulting from both the correlated and uncorrelated noise, giving Eq. (2) in the main text.

APPENDIX J: EXPECTED PEARSON CORRELATIONS FROM PHASE-RANDOM MONOCHROMATIC NOISE

Figure 6(c) shows the measured magnetic noise correlators from multiplexed covariance magnetometry versus the expected correlator values from theory. To determine the expected correlations, we first measure local noise at each NV center by measuring spin coherence with an *XY*8 sequence as a function of the amplitude of the applied noise [41]; the theory for this curve is shown in blue in Fig. 16. These measurements allow us to determine the expected correlation amplitude for a chosen noise amplitude [34], plotted in red in Fig. 16.

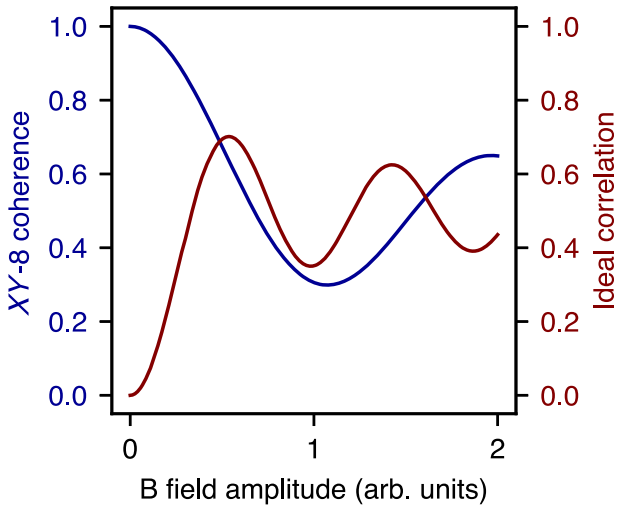


FIG. 16. Expected correlation amplitudes from magnetic noise. NV center *XY*8 coherence and ideal two-point correlation amplitude for varying magnetic field noise amplitude.

[1] J. M. Taylor, P. Cappellaro, L. Childress, L. Jiang, D. Budker, P. R. Hemmer, A. Yacoby, R. Walsworth, and M. D. Lukin, *High-sensitivity diamond magnetometer with nanoscale resolution*, Nat. Phys. **4**, 810 (2008).

[2] J. R. Maze, P. L. Stanwix, J. S. Hodges, S. Hong, J. M. Taylor, P. Cappellaro, L. Jiang, M. V. G. Dutt, E. Togan, A. S. Zibrov, A. Yacoby, R. L. Walsworth, and M. D. Lukin, *Nanoscale magnetic sensing with an individual electronic spin in diamond*, Nature (London) **455**, 644 (2008).

[3] I. Lovchinsky, A. O. Sushkov, E. Urbach, N. P. de Leon, S. Choi, K. De Greve, R. Evans, R. Gertner, E. Bersin, C. Müller, L. McGuinness, F. Jelezko, R. L. Walsworth, H. Park, and M. D. Lukin, *Nuclear magnetic resonance detection and spectroscopy of single proteins using quantum logic*, Science **351**, 836 (2016).

[4] G. Kucsko, P. C. Maurer, N. Y. Yao, M. Kubo, H. J. Noh, P. K. Lo, H. Park, and M. D. Lukin, *Nanometre-scale thermometry in a living cell*, Nature (London) **500**, 54 (2013).

[5] S. Kolkowitz, Q. P. Unterreithmeier, S. D. Bennett, and M. D. Lukin, *Sensing distant nuclear spins with a single electron spin*, Phys. Rev. Lett. **109**, 137601 (2012).

[6] F. Dolde, H. Fedder, M. W. Doherty, T. Nöbauer, F. Rempp, G. Balasubramanian, T. Wolf, F. Reinhard, L. C. L. Hollenberg, F. Jelezko, and J. Wrachtrup, *Electric-field sensing using single diamond spins*, Nat. Phys. **7**, 459 (2011).

[7] L. V. H. Rodgers, S. T. Nguyen, J. H. Cox, K. Zervas, Z. Yuan, S. Sangtawesin, A. Stacey, C. Jaye, C. Weiland, A. Pershin, A. Gali, L. Thomsen, S. A. Meynell, L. B. Hughes, A. C. B. Jayich, X. Gui, R. J. Cava, R. R. Knowles, and N. P. de Leon, *Diamond surface functionalization via visible light–driven C–H activation for nanoscale quantum sensing*, Proc. Natl. Acad. Sci. U.S.A. **121**, e2316032121 (2024).

[8] M. Sutula, I. Christen, E. Bersin, M. P. Walsh, K. C. Chen, J. Mallek, A. Melville, M. Titze, E. S. Bielejec, S. Hamilton, D. Braje, P. B. Dixon, and D. R. Englund, *Large-scale optical characterization of solid-state quantum emitters*, Nat. Mater. **22**, 1338 (2023).

[9] L. Childress, M. V. Gurudev Dutt, J. M. Taylor, A. S. Zibrov, F. Jelezko, J. Wrachtrup, P. R. Hemmer, and M. D. Lukin, *Coherent dynamics of coupled electron and nuclear spin qubits in diamond*, Science **314**, 281 (2006).

[10] E. Marchiori, L. Ceccarelli, N. Rossi, L. Lorenzelli, C. L. Degen, and M. Poggio, *Nanoscale magnetic field imaging for 2D materials*, Nat. Rev. Phys. **4**, 49 (2022).

[11] P. Maletinsky, S. Hong, M. S. Grinolds, B. Hausmann, M. D. Lukin, R. L. Walsworth, M. Loncar, and A. Yacoby, *A robust scanning diamond sensor for nanoscale imaging with single nitrogen-vacancy centres*, Nat. Nanotechnol. **7**, 320 (2012).

[12] A. Ariyaratne, D. Bluvstein, B. A. Myers, and A. C. B. Jayich, *Nanoscale electrical conductivity imaging using a nitrogen-vacancy center in diamond*, Nat. Commun. **9**, 2406 (2018).

[13] D. R. Glenn, D. B. Bucher, J. Lee, M. D. Lukin, H. Park, and R. L. Walsworth, *High-resolution magnetic resonance spectroscopy using a solid-state spin sensor*, Nature (London) **555**, 351 (2018).

[14] D. R. Glenn, R. R. Fu, P. Kehayias, D. Le Sage, E. A. Lima, B. P. Weiss, and R. L. Walsworth, *Micrometer-scale magnetic imaging of geological samples using a quantum diamond microscope*, Geochem. Geophys. Geosyst. **18**, 3254 (2017).

[15] J. F. Barry, M. J. Turner, J. M. Schloss, D. R. Glenn, Y. Song, M. D. Lukin, H. Park, and R. L. Walsworth, *Optical magnetic detection of single-neuron action potentials using quantum defects in diamond*, Proc. Natl. Acad. Sci. U.S.A. **113**, 14133 (2016).

[16] Z. Kazi, I. M. Shelby, R. Nirodi, J. Turnbull, H. Watanabe, K. M. Itoh, P. A. Wiggins, and Kai-Mei C. Fu, *Direct measurement of DNA bending by quantum magnetic imaging of a nanomechanical torque balance*, Phys. Rev. Appl. **22**, 064044 (2024).

[17] L. M. Pham, S. J. DeVience, F. Casola, I. Lovchinsky, A. O. Sushkov, E. Bersin, J. Lee, E. Urbach, P. Cappellaro, H. Park, A. Yacoby, M. Lukin, and R. L. Walsworth, *NMR technique for determining the depth of shallow nitrogen-vacancy centers in diamond*, Phys. Rev. B **93**, 045425 (2016).

[18] S. Sangtawesin, B. L. Dwyer, S. Srinivasan, J. J. Allred, L. V. H. Rodgers, K. De Greve, A. Stacey, N. Dontschuk, K. M. O'Donnell, D. Hu, D. A. Evans, C. Jaye, D. A. Fischer, M. L. Markham, D. J. Twitchen, H. Park, M. D. Lukin, and N. P. de Leon, *Origins of diamond surface noise probed by correlating single-spin measurements with surface spectroscopy*, Phys. Rev. X **9**, 031052 (2019).

[19] Z. Yuan, M. Fitzpatrick, L. V. H. Rodgers, S. Sangtawesin, S. Srinivasan, and N. P. de Leon, *Charge state dynamics and optically detected electron spin resonance contrast of shallow nitrogen-vacancy centers in diamond*, Phys. Rev. Res. **2**, 033263 (2020).

[20] M. W. Doherty, N. B. Manson, P. Delaney, F. Jelezko, J. Wrachtrup, and L. C. L. Hollenberg, *The nitrogen-vacancy colour centre in diamond*, Phys. Rep. **528**, 1 (2013).

[21] J. F. Barry, J. M. Schloss, E. Bauch, M. J. Turner, C. A. Hart, L. M. Pham, and R. L. Walsworth, *Sensitivity optimization for NV-diamond magnetometry*, Rev. Mod. Phys. **92**, 015004 (2020).

[22] Z. Kazi, I. M. Shelby, H. Watanabe, K. M. Itoh, V. Shutthanandan, P. A. Wiggins, and Kai-Mei C. Fu, *Wide-field dynamic magnetic microscopy using double-double quantum driving of a diamond defect ensemble*, Phys. Rev. Appl. **15**, 054032 (2021).

[23] J. Rovny, S. Gopalakrishnan, A. C. B. Jayich, P. Maletinsky, E. Demler, and N. P. de Leon, *Nanoscale diamond quantum sensors for many-body physics*, Nat. Rev. Phys. **6**, 753 (2024).

[24] F. Machado, E. A. Demler, N. Y. Yao, and S. Chatterjee, *Quantum noise spectroscopy of dynamical critical phenomena*, Phys. Rev. Lett. **131**, 070801 (2023).

[25] R. Xue, N. Maksimovic, P. E. Dolgirev, L.-Q. Xia, R. Kitagawa, A. Müller, F. Machado, D. R. Klein, D. MacNeill, K. Watanabe, T. Taniguchi, P. Jarillo-Herrero, M. D. Lukin, E. Demler, and A. Yacoby, *Signatures of magnon hydrodynamics in an atomically-thin ferromagnet*, arXiv:2403.01057.

[26] T. I. Andersen, B. L. Dwyer, J. D. Sanchez-Yamagishi, J. F. Rodriguez-Nieva, K. Agarwal, K. Watanabe, T. Taniguchi, E. A. Demler, P. Kim, H. Park, and M. D. Lukin, *Electron-phonon instability in graphene revealed by global and local noise probes*, Science **364**, 154 (2019).

[27] Y. Zhang, R. Samajdar, and S. Gopalakrishnan, *Nanoscale sensing of spatial correlations in nonequilibrium current noise*, arXiv:2404.15398.

[28] M. E. Ziffer *et al.*, *Quantum noise spectroscopy of critical slowing down in an atomically thin magnet*, arXiv:2407.05614.

[29] Y. Li, Z. Ding, C. Wang, H. Sun, Z. Chen, P. Wang, Y. Wang, M. Gong, H. Zeng, F. Shi, and J. Du, *Critical fluctuation and noise spectra in two-dimensional* Fe_3GeTe_2 *magnets*, arXiv:2407.00647.

[30] S. Chatterjee, J. F. Rodriguez-Nieva, and E. Demler, *Diagnosing phases of magnetic insulators via noise magnetometry with spin qubits*, Phys. Rev. B **99**, 104425 (2019).

[31] Z. Yuan, S. Mukherjee, J. D. Thompson, N. P. de Leon, A. Gardill, and S. Kolkowitz, *An instructional lab apparatus for quantum experiments with single nitrogen-vacancy centers in diamond*, Am. J. Phys. **92**, 892 (2024).

[32] M. Cai, Z. Guo, F. Shi, C. Li, M. Wang, W. Ji, P. Wang, and J. Du, *Parallel optically detected magnetic resonance spectrometer for dozens of single nitrogen-vacancy centers using laser-spot lattice*, Rev. Sci. Instrum. **92**, 045107 (2021).

[33] D. Bluvstein, Z. Zhang, and Ania C. Bleszynski Jayich, *Identifying and mitigating charge instabilities in shallow diamond nitrogen-vacancy centers*, Phys. Rev. Lett. **122**, 076101 (2019).

[34] J. Rovny, Z. Yuan, M. Fitzpatrick, A. I. Abdalla, L. Futamura, C. Fox, M. C. Cambria, S. Kolkowitz, and N. P. De Leon, *Nanoscale covariance magnetometry with diamond quantum sensors*, Science **378**, 1301 (2022).

[35] B. L. Shields, Q. P. Unterreithmeier, N. P. de Leon, H. Park, and M. D. Lukin, *Efficient readout of a single spin state in diamond via spin-to-charge conversion*, Phys. Rev. Lett. **114**, 136402 (2015).

[36] F. Nogrette, H. Labuhn, S. Ravets, D. Barredo, L. Béguin, A. Vernier, T. Lahaye, and A. Browaeys, *Single-atom trapping in holographic 2D arrays of microtraps with arbitrary geometries*, Phys. Rev. X **4**, 021034 (2014).

[37] A. G. Basden, C. A. Haniff, and C. D. Mackay, *Photon counting strategies with low-light-level CCDs*, Mon. Not. R. Astron. Soc. **345**, 985 (2003).

[38] N. Aslam, G. Waldherr, P. Neumann, F. Jelezko, and J. Wrachtrup, *Photo-induced ionization dynamics of the nitrogen vacancy defect in diamond investigated by single-shot charge state detection*, New J. Phys. **15**, 013064 (2013).

[39] D. Wirtitsch, G. Wachter, S. Reisenbauer, M. Gulka, V. Ivády, F. Jelezko, A. Gali, M. Nesladek, and M. Trupke, *Exploiting ionization dynamics in the nitrogen vacancy center for rapid, high-contrast spin, and charge state initialization*, Phys. Rev. Res. **5**, 013014 (2023).

[40] S. Meiboom and D. Gill, *Modified spin-echo method for measuring nuclear relaxation times*, Rev. Sci. Instrum. **29**, 688 (1958).

[41] C. L. Degen, F. Reinhard, and P. Cappellaro, *Quantum sensing*, Rev. Mod. Phys. **89**, 035002 (2017).

[42] J. Rovny, S. Kolkowitz, and N. P. d. Leon, *Multi-qubit nanoscale sensing with entanglement as a resource*, arXiv:2504.12533.

[43] L. Thiel, Z. Wang, M. A. Tschudin, D. Rohner, I. Gutiérrez-Lezama, N. Ubrig, M. Gibertini, E. Giannini, A. F. Morpurgo, and P. Maletinsky, *Probing magnetism in 2D materials at the nanoscale with single-spin microscopy*, Science **364**, 973 (2019).

[44] M. J. H. Ku, T. X. Zhou, Q. Li, Y. J. Shin, J. K. Shi, C. Burch, L. E. Anderson, A. T. Pierce, Y. Xie, A. Hamo, U. Vool, H. Zhang, F. Casola, T. Taniguchi, K. Watanabe, M. M. Fogler, P. Kim, A. Yacoby, and R. L. Walsworth, *Imaging viscous flow of the Dirac fluid in graphene*, Nature (London) **583**, 537 (2020).

[45] A. Jenkins, S. Baumann, H. Zhou, S. A. Meynell, Y. Daipeng, K. Watanabe, T. Taniguchi, A. Lucas, A. F. Young, and A. C. Bleszynski Jayich, *Imaging the breakdown of ohmic transport in graphene*, Phys. Rev. Lett. **129**, 087701 (2022).

[46] U. Vool, A. Hamo, G. Varnavides, Y. Wang, T. X. Zhou, N. Kumar, Y. Dovzhenko, Z. Qiu, C. A. C. Garcia, A. T. Pierce, J. Gooth, P. Anikeeva, C. Felser, P. Narang, and A. Yacoby, *Imaging phonon-mediated hydrodynamic flow in* WTe_2, Nat. Phys. **17**, 1216 (2021).

[47] L. Thiel, D. Rohner, M. Ganzhorn, P. Appel, E. Neu, B. Müller, R. Kleiner, D. Koelle, and P. Maletinsky, *Quantitative nanoscale vortex imaging using a cryogenic quantum magnetometer*, Nat. Nanotechnol. **11**, 677 (2016).

[48] S. Chen, S. Park, U. Vool, N. Maksimovic, D. A. Broadway, M. Flaks, T. X. Zhou, P. Maletinsky, A. Stern, B. I. Halperin, and A. Yacoby, *Current induced hidden states in Josephson junctions*, Nat. Commun. **15**, 8059 (2024).

[49] S. Kolkowitz, A. Safira, A. A. High, R. C. Devlin, S. Choi, Q. P. Unterreithmeier, D. Patterson, A. S. Zibrov, V. E. Manucharyan, H. Park, and M. D. Lukin, *Probing Johnson noise and ballistic transport in normal metals with a single-spin qubit*, Science **347**, 1129 (2015).

[50] B. L. Dwyer, L. V. H. Rodgers, E. K. Urbach, D. Bluvstein, S. Sangtawesin, H. Zhou, Y. Nassab, M. Fitzpatrick, Z. Yuan, K. De Greve, E. L. Peterson, H. Knowles, T. Sumarac, J.-P. Chou, A. Gali, V. V. Dobrovitski, M. D. Lukin, and N. P. de Leon, *Probing spin dynamics on diamond surfaces using a single quantum sensor*, PRX Quantum **3**, 040328 (2022).

[51] K. Agarwal, R. Schmidt, B. Halperin, V. Oganesyan, G. Zaránd, M. D. Lukin, and E. Demler, *Magnetic noise spectroscopy as a probe of local electronic correlations in two-dimensional systems*, Phys. Rev. B **95**, 155107 (2017).

[52] A. Lucas and K. C. Fong, *Hydrodynamics of electrons in graphene*, J. Phys. Condens. Matter **30**, 053001 (2018).

[53] J. B. Curtis, N. Maksimovic, N. R. Poniatowski, A. Yacoby, B. Halperin, P. Narang, and E. Demler, *Probing the Berezinskii-Kosterlitz-Thouless vortex unbinding transition in two-dimensional superconductors using local noise magnetometry*, Phys. Rev. B **110**, 144518 (2024).

[54] Q. Chen, Z. Wang, R. Boyack, S. Yang, and K. Levin, *When superconductivity crosses over: From BCS to BEC*, Rev. Mod. Phys. **96**, 025002 (2024).

[55] C. Broholm, R. J. Cava, S. A. Kivelson, D. G. Nocera, M. R. Norman, and T. Senthil, *Quantum spin liquids*, Science **367**, eaay0668 (2020).

[56] M. Cambria, S. Chand, C. M. Reiter, and S. Kolkowitz, following paper, *Scalable parallel measurement of individual nitrogen-vacancy centers*, Phys. Rev. X **15**, 031015 (2025).

[57] D. Kim, A. Keesling, A. Omran, H. Levine, H. Bernien, M. Greiner, M. D. Lukin, and D. R. Englund, *Large-scale uniform optical focus array generation with a phase spatial light modulator*, Opt. Lett. **44**, 3178 (2019).